Three-dimensional filling flow into a model left ventricle

By F. DOMENICHINI[1], G. PEDRIZZETTI[2] AND B. BACCANI[1]

[1]Dipartimento di Ingegneria Civile, Università di Firenze, Via S. Marta 3, 50139 Firenze, Italy
[2]Dipartimento di Ingegneria Civile, Università di Trieste, P.le Europa 1, 34127 Trieste, Italy

A numerical study of the three-dimensional fluid dynamics inside a model left ventricle during diastole is presented. The ventricle is modelled as a portion of a prolate spheroid with a moving wall, whose dynamics is externally forced to agree with a simplified waveform of the entering flow. The flow equations are written in the meridian body-fitted system of coordinates, and expanded in the azimuthal direction using the Fourier representation. The harmonics of the dependent variables are normalized in such a way that they automatically satisfy the high-order regularity conditions of the solution at the singular axis of the system of coordinates. The resulting equations are solved numerically using a mixed spectral–finite differences technique. The flow dynamics is analysed by varying the governing parameters, in order to understand the main fluid phenomena in an expanding ventricle, and to obtain some insight into the physiological pattern commonly detected. The flow is characterized by a well-defined structure of vorticity that is found to be the same for all values of the parameters, until, at low values of the Strouhal number, the flow develops weak turbulence.

1. Introduction

The physically based modelling of biological flows has received growing attention in the last years. Specifically, the enormous increase of available data that can be obtained by the current diagnostic tools requires the development of interpretative schemes to allow data synthesis and to improve the understanding of the physical processes involved. Cardiac dynamics represents a central such issue given its physiological relevance. However, the fluid dynamics in the heart cavities, and the fluid–tissue interaction, present several modelling difficulties and understanding is still far from being satisfactory.

Several recent studies have focused on the left ventricle filling dynamics (diastole), which is known to play an important role in the heart functionality (Mandinov *et al.* 2000; Vasan & Levy 2002) and which presents a rich fluid dynamics. From experimental (Steen & Steen 1994) and numerical results (Vierendeels *et al.* 2000; Baccani, Domenichini & Pedrizzetti 2002*a*), limited to an axisymmetric picture, the principal features of the left ventricle diastolic filling have been described. During the early phase, the flow that enters the ventricle from the atrium through the mitral valve (the mitral jet) develops compact ring-shaped vortex structures, which rapidly interact with the wall boundary layer while travelling towards the ventricular apex where they eventually dissipate. Such experimental and numerical results have been compared with clinical observations by evaluating the velocity on a one-dimensional space subset along the ventricle axis, and constructing the space–time map of the axial velocity. The analysis in terms of this reduced representation, which is common in echo-Doppler

diagnostic imaging (transmitral M-mode; Garcia, Thomas & Klein 1998), suggests the interpretation of diagnostic images in terms of vortex dynamics (Baccani *et al.* 2002*b*; Vierendeels, Dick & Verdonck 2002). In the same axisymmetric framework, the influence of the mitral valve at the ventricular entrance was also studied (Baccani, Domenichini & Pedrizzetti 2003), showing how the indicators commonly extracted by clinicians are also related to the valvular opening motion.

The axisymmetric modelling gives some preliminary understanding of the ventricular flow, but it is not a realistic enough approximation for the interpretation of the phenomena that are present in most circumstances. The actual dynamics is far from being axisymmetric. From flow visualizations (Bellhouse 1972; Reul, Talukder & Muller 1981; Wieting & Stripling 1984) it appears that the vortex-ring-like structure forming at the mitral entrance rapidly deforms, depending on the different shapes and sizes of the valvular leaflets. The entering structure develops with a large vortex located behind the longer valvular leaflet and a smaller one on the opposite side. The larger circulation cell persists during the following contraction phase (systole) possibly facilitating blood ejection from the ventricle to the aorta. Such a flow pattern also avoids the stagnation of fluid at the cavity apex that could induce negative physiological consequences (thrombus). This description is based on a two-dimensional view looking at the flow picture on a plane cross-section, while the structure of the corresponding three-dimensional flow is still unclear. A related study of the three-dimensional flow entering a circular duct through an eccentric orifice (Bolzon, Zovatto & Pedrizzetti 2003) has shown how the presence of a small eccentricity drives the flow away from the axisymmetric solution.

The numerical solution of the ventricular flow presents several difficulties due to the moving boundary and the flow–wall interaction, which are of primary relevance in closed cavity problems. The fluid dynamics phenomena that participate are intense: the inflow is an impulsive jet that enters a cavity a few centimetres long with a velocity near to $1\,\mathrm{m\,s^{-1}}$, and that almost instantaneously reaches the ventricle moving wall and interacts with it.

A first numerical solution based on the finite volumes method, forced by a quasi-stationary wall motion, was proposed by Taylor & Yamaguchi (1995). There a realistic (dog) ventricular geometry was prepared *a priori*, defining a set of configurations which change at given instants of time and are kept constant in between; the fluid equations were integrated during these intervals of time imposing a flow through the wall. Recently, a coupled magnetic resonance imaging–computational fluid dynamics (MRI-CFD) study on a realistic heart was performed by Saber *et al.* (2001); there the gross features of the flow are captured and the development of secondary flow is shown. However, the work is primarily intended to show the feasibility of the MRI-CFD approach; the results are not analysed in a fluid dynamics perspective and suffer, as admitted by the authors, from insufficient accuracy in the resolution and some limitations in the boundary condition modelling. A more recent work (Nakamura *et al.* 2003) presents some insights into the three-dimensional left ventricle flow, but the reported results seem to be limited by the dominance of the numerical viscous effects resulting from the continuous remeshing procedure and by the coarseness of the numerical grid.

An alternative method for the coupled solution of the fluid–wall problem has been developed by introducing the concept of immersed boundary elements (IBE). In the IBE method the fluid problem is solved on a regular domain (typically a periodic box), with a distribution of fictitious body forces. These replace the presence of the wall, which in turn moves with the fluid by an iterative procedure (see Peskin &

McQueen 1989*a*, *b* for details). Such an approach is well-suited to reproducing the valve dynamics and it also has a generality of application in arbitrarily complex three-dimensional geometries. On the other hand, the method presents a reduced accuracy in the boundary layers, because the wall does not lie on coordinate curves, where interpolating/spreading procedures are necessary to transform Eulerian (fluid) quantities to Lagrangian (solid) ones, and vice versa. This method has been applied to the dynamics of the left heart (Lemmon & Yoganathan 2000; McQueen & Peskin 2000), where the gross phenomena due to the fluid–tissue interaction are reproduced.

This work is devoted to the numerical modelling and an initial understanding of the three-dimensional structure of the flow entering a ventricular-shaped cavity. Extending the axisymmetric model of Baccani *et al.* (2002*a*), the ventricular geometry is taken as that of a prolate spheroid with moving walls. The proper connection of the left ventricular model with the cardiovascular system requires the quantification of several parameters, including the thick-tissue time-varying mechanical properties and a reference pressure time profile, or parameters of a general lumped model. Given the difficulty in obtaining realistic data for such quantities (Stevens *et al.* 2003), we force the system with the dynamics of the walls that are easily accessed in routine ultrasound measurements, and that are directly related to the time-law of the entering discharge.

The flow equations are written in the moving body-fitted system of coordinates, and expanded in the azimuthal direction using Fourier series. Particular care is taken in defining a mathematical well-posed problem about the singular axis of the prolate spheroid coordinate system. For this, a normalization of the variables is introduced following a method previously developed by the authors in cylindrical coordinates (Domenichini & Baccani 2004), which allows the appropriate definition of the boundary and regularity conditions for the Fourier harmonics at the singular axis. A mixed spectral–finite differences numerical method is thus used, allowing enhanced resolution at the ventricle wall and close to the inlet section, where significant vorticity gradients are expected.

The flow structure is analysed starting from conditions that depart from the axisymmetric case and move towards more realistic ones. The flow parameters are varied within the physiological range, from young heart conditions towards values of the Reynolds number when the development of weak turbulence is expected. The mathematical formulation and the numerical method are reported in §2 and §3, respectively; results are discussed in §4, and concluding remarks can be found in §5.

2. Mathematical formulation

The mathematical formulation starts from that reported in Baccani *et al.* (2002*a*) for the axisymmetric case, where the moving prolate spheroid system of coordinates is introduced. The flow domain is half of a prolate spheroid; its geometry is defined by the temporal functions $D(t)$ and $H(t)$, that is the time variation of the equatorial plane diameter and of the major semiaxis, respectively, as sketched in figure 1.

The domain is described by the system of prolate spheroidal moving coordinates $\{\mu, \eta, \theta\}$, where $\mu \in [0, 1]$, $\eta \in [0, \pi/2]$, and $\theta \in [0, 2\pi]$; μ and η map the meridian plane, θ is the cylindrical azimuthal coordinate. The cavity wall corresponds to the coordinate surface $\mu = 1$, and the mitral (inlet) plane to $\eta = \pi/2$. The relationship between the chosen system of coordinates and the cylindrical ones $\{z, r, \theta\}$ is

$$\left.\begin{aligned} r &= \delta(t) \sinh(\alpha(t)\mu) \sin \eta, \\ z &= \delta(t) \cosh(\alpha(t)\mu) \cos \eta, \\ \theta &= \theta. \end{aligned}\right\} \tag{1}$$
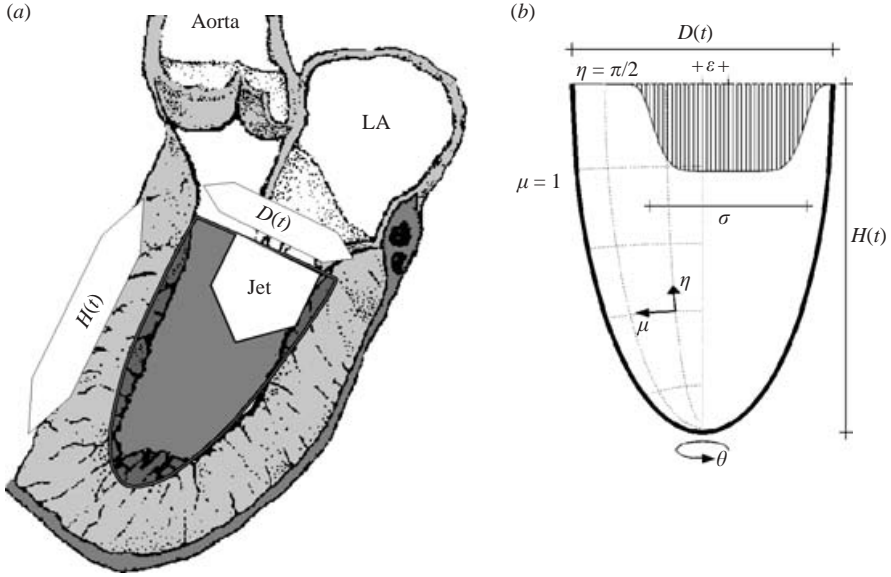
FIGURE 1. Sketch of (*a*) the physical problem and (*b*) of the mathematical model.

The time-varying functions $\alpha(t)$ and $\delta(t)$ are related to $H(t)$ and $D(t)$ by

$$\delta = (H^2 - D^2/4)^{1/2}, \quad \alpha = \tanh^{-1}(D/2H); \tag{2}$$

in the present case we assume a fixed ratio $H/D = 2$, that is $\tanh(\alpha) = 0.25$. Typically this ratio oscillates weakly around this value during the cardiac cycle, such a variation is usually different for each case. Once the time variation of the ventricle volume $V(t)$ is known, e.g. once the entering discharge is specified, the function $D(t)$, and consequently $H(t)$, can be easily derived using geometrical considerations, and from these $\delta(t)$ is obtained.

The metric coefficients of the coordinates system are

$$h_\mu = \alpha h_\eta, \quad h_\eta = \delta\sqrt{\cosh^2(\alpha\mu) - \cos^2\eta}, \quad h_\theta = \delta\sinh(\alpha\mu)\sin\eta, \tag{3}$$

where the time dependence is omitted for brevity. This system of coordinates describes a moving object in the physical space; therefore a fixed point in the $\{\mu, \eta, \theta\}$ space has a physical velocity $\boldsymbol{c}$, whose components can be written in the general case as

$$c_\mu = \dot{\delta}\frac{\delta\alpha}{h_\mu}\sinh(\alpha\mu)\cosh(\alpha\mu) + \mu h_\mu\frac{\dot{\alpha}}{\alpha}, \quad c_\eta = -\dot{\delta}\frac{\delta}{h_\eta}\sin\eta\cos\eta, \quad c_\theta = 0, \tag{4}$$

where the dot indicates time derivative. In the present case, the expression for c_μ simplifies, since $\dot{\alpha} = 0$.

The dimensionless Navier–Stokes and continuity equations are written as

$$\frac{\partial\boldsymbol{v}}{\partial t} + \boldsymbol{\omega}\times(\boldsymbol{v}-\boldsymbol{c}) + \boldsymbol{v}\cdot\nabla\boldsymbol{c} = -\nabla\phi - \frac{1}{\beta}\nabla\times\boldsymbol{\omega}, \tag{5a}$$

$$\nabla\cdot\boldsymbol{v} = 0. \tag{5b}$$

The vectors $\boldsymbol{v}$ and $\boldsymbol{\omega}$ are the velocity and vorticity, respectively, and $\boldsymbol{c}$ is the velocity of the system of coordinates defined in (4); they are all measured with respect to the laboratory frame, expressed as functions of $\{\mu, \eta, \theta\}$. It is important to point out that

the spatial differential operators in (5a) are written in the curvilinear system $\{\mu, \eta, \theta\}$ defined in (1); equally the time derivative is not taken at a fixed position but at fixed values of these coordinates. The scalar field ϕ represents the irrotational contribution to the flow, that is $\phi = p + v^2/2 - \boldsymbol{c} \cdot \boldsymbol{v}$, where p is the dimensionless pressure field and v is the velocity modulus. To write (5a), the differential identity

$$\boldsymbol{c} \cdot \nabla \boldsymbol{v} = \boldsymbol{\omega} \times \boldsymbol{c} + (\nabla \times \boldsymbol{c}) \times \boldsymbol{v} - \boldsymbol{v} \cdot \nabla \boldsymbol{c} + \nabla(\boldsymbol{c} \cdot \boldsymbol{v})$$

has been used; it can be easily verified from (4) that, assuming $\dot{\alpha} = 0$, $\nabla \times \boldsymbol{c} = 0$ and $\boldsymbol{v} \cdot \nabla \boldsymbol{c} = \dot{\delta} \boldsymbol{v}/\delta$. The general form of the differential operators in (5) for an orthogonal system of coordinates can be found in Batchelor (1967), and Morse & Feshbach (1953).

The diameter $D_0 = D(t=0)$ at the beginning of the diastolic filling phase is chosen as reference lengthscale. The timescale T is the heartbeat period; thus we have a Stokes number $\beta = D_0^2/\nu T$, ν being the kinematic viscosity of the fluid. The diastolic phase analysed here has therefore a dimensionless duration approximately equal to 0.5.

The system is forced with a given time law of the entering discharge; a simple analytical form is chosen, that reproduces the rapid acceleration and slower deceleration of a flow pulsation inside the heart chambers and principal arterial vessels. It is represented by the dimensionless function

$$\mathcal{Q}(t) = A(St)t^2 \exp(-ft); \tag{6}$$

$f = 20$ is the characteristic frequency of the deceleration, giving a peak time $t_p = 0.1$. The function $A(St)$ that scales the total discharge depends on the Strouhal number $St = D_0/UT$; the scale U is the velocity at the inlet section, $\eta = \pi/2$, corresponding to the peak value of the discharge $\mathcal{Q}_p = \mathcal{Q}(t_p)$, averaged on the area effectively occupied by the entering jet. The following eccentric blunt velocity profile v_η is assigned at the inlet:

$$v_\eta(\mu, \theta) = C(t) \exp\left[-\left(\frac{(r\cos\theta - \varepsilon)^2 + (r\sin\theta)^2}{\sigma^2}\right)^4\right] \text{ at } \eta = \pi/2; \tag{7}$$

ε is the eccentricity of the profile, σ controls the ratio between the entering jet and the diameter $D(t)$, C is the normalization coefficient to agree with the integral (6). From (7), the velocity scale is $U = 4\mathcal{Q}_p/\pi(\sigma D_0)^2$.

Realistic values for the parameters are $\sigma \simeq 0.6$ to 0.7, and $\varepsilon \simeq 0.1$ to 0.15, see figure 1; in the present work, a fixed value $\sigma = 0.6$ has been used, therefore $A = 209/St$. The scaling quantities are chosen for their physical significance, and also following the values commonly measured in clinical practice. Typical dimensional values in healthy young adults are $T \simeq 0.8$ s to 1 s, corresponding to 75 and 60 heartbeats per minute, U is about 0.5 m s^{-1} or little above it, and D_0 from 0.02 to 0.025 m. From these values, the Stokes parameter β ranges between 120 and 250, assuming $\nu \simeq 3.3 \times 10^{-6}$ m^2 s^{-1}, and St can be assumed between 0.03 and 0.075. A peak Reynolds number can be defined as $Re = UD_0/\nu = \beta/St$.

From (5a), the derivation of the three scalar momentum balances along the coordinate directions is tedious but straightforward. Then, any variable is expanded in Fourier series along θ as $f(\mu, \eta, \theta, t) = \sum f_n(\mu, \eta, t)\, e^{in\theta}$, where the f_n are complex functions and i is the imaginary unit. The introduction of the Fourier expansions into (5) gives the evolution equations for the harmonics of the velocity components, and the corresponding mass conservation laws.

The system of equations obtained is completed with the boundary conditions. At the wall, the fluid velocity vector is equal to that at the wall (4). At the mitral plane,

the profile (7) of the normal velocity v_η is imposed with a zero normal derivative condition for the other velocity components.

The singular axis, $r = 0$ in cylindrical coordinates, corresponds in the present system to the coordinate curves $\mu = 0$ and $\eta = 0$; its treatment requires particular attention, because the condition of continuity of the variables and their derivatives must be guaranteed by the spectral representation. In particular, the regularity of the spectral solution requires imposing conditions on the nth harmonic up to the nth derivative (Lewis & Bellan 1990; Lopez, Marques & Shen 2002) as follows. At $\mu = 0$,

$$\left.\begin{aligned}
\frac{\partial^k v_{\eta n}}{\partial \mu^k} &= 0 && \text{for } k = 0, 1, \ldots, n-1, \\
\frac{\partial^k v_{\mu n}}{\partial \mu^k} &= \frac{\partial^k v_{\theta n}}{\partial \mu^k} = 0 && \text{for } k = 0, 1, \ldots, n-2, n,
\end{aligned}\right\} \tag{8}$$

where $n > 0$; the case $n = 0$ is recovered from the axisymmetric case, giving $\partial v_{\eta 0}/\partial \mu = v_{\mu 0} = v_{\theta 0} = 0$. Analogous expressions, exchanging μ and η, hold at $\eta = 0$.

Several methods have been suggested for the accurate description of the flow close to the symmetry axis taking into account conditions (8) (Constantinescu & Lele 2002, and references therein). In the present work we generalize the approach previously developed in cylindrical coordinates (Domenichini & Baccani 2004), where the flow variables are normalized with the distance from the singular axis. In that work, the velocity harmonics, e.g. v_{kn} where k stands for the components $\{z, r, \theta\}$, are substituted by normalized ones, g_{kn}, defined by $v_{kn} = g_{kn} r^{|n|-1}$. The generalization to the present case is performed by considering that the radial distance $r = \delta \sinh(\alpha\mu) \sin \eta$ defined in (1) behaves close to the axis as $r \sim \mu$ when $\mu \to 0$, and as $r \sim \eta$ when $\eta \to 0$. It follows that a natural definition of scaled harmonics for this case is

$$v_{kn}(\mu, \eta) = g_{kn}(\mu, \eta)\mu^{|n|-1}\eta^{|n|-1}, \tag{9}$$

where $n \neq 0$, and k stands for $\{\mu, \eta, \theta\}$. Along the same lines, a pseudopotential Q is introduced to normalize ϕ in (5a), as

$$\phi_n(\mu, \eta) = Q_n(\mu, \eta)\mu^{|n|}\eta^{|n|}, \tag{10}$$

and the scaled vorticity field is defined by

$$\omega_{kn}(\mu, \eta) = q_{kn}(\mu, \eta)\mu^{|n|-2}\eta^{|n|-2}. \tag{11}$$

For the zeroth mode, the formulation in terms of primitive variables is left unchanged (Baccani *et al.* 2002a).

The normalization is a method to account for the high-order conditions (8) that, when recast in terms of the scaled variables, become

$$g_{\eta n} = 0, \quad \frac{\partial g_{\mu n}}{\partial \mu} = \frac{\partial g_{\theta n}}{\partial \mu} = 0, \tag{12}$$

and similarly at $\eta = 0$. These are conditions up to the first order, and they can be directly satisfied as boundary conditions in the (scaled) Navier–Stokes equations. The conditions (12) on the normalized variables correspond to the high-order conditions (8) on the primitive variables. Conditions for the harmonics Q_n and q_{kn} are derived from (12):

$$\frac{\partial Q_n}{\partial \mu} = 0 \text{ at } \mu = 0, \quad \frac{\partial Q_n}{\partial \eta} = 0 \text{ at } \eta = 0, \tag{13}$$

$$q_{kn} = 0 \text{ at } \mu = 0 \text{ and at } \eta = 0. \tag{14}$$

Once the normalizations (9)–(11) have been introduced, the differential operators can be rewritten to obtain the relationships between the normalized fields. A formal curl operator relating the harmonics q_{kn} to the g_{kn} ones is defined giving, as an example for $q_{\mu n}$,

$$q_{\mu n} = \frac{\mu \eta}{h_\eta h_\theta} \left[\eta \frac{\partial}{\partial \eta} \left(\frac{g_{\theta n} h_\theta}{\eta} \right) + \frac{n g_{\theta n} h_\theta}{\eta} - i n g_\eta h_\eta \right]. \tag{15}$$

Following the same lines, a formal gradient operator which gives an irrotational contribution to the g field when applied to the pseudopotential Q is

$$g_{\mu n} = \frac{\eta}{h_\mu} \left(\mu \frac{\partial Q_n}{\partial \mu} + n Q_n \right), \qquad g_{\eta n} = \frac{\mu}{h_\eta} \left(\eta \frac{\partial Q_n}{\partial \eta} + n Q_n \right), \qquad g_{\eta n} = \frac{i n Q_n \mu \eta}{h_\theta}. \tag{16}$$

Note that definitions (15)–(16) automatically satisfy the differential identity $\nabla \times \nabla \phi = 0$, when rewritten in terms of the normalised variables. The same procedure is followed to define a formal divergence operator.

Once the scalar form of the Navier–Stokes equation (5a) has been projected into the Fourier space, and the primitive variables and operators have been substituted accordingly with (9)–(16), the equations to be solved become, after some manipulations,

$$\left. \begin{aligned} \frac{\partial g_{\mu n}}{\partial t} + G_{\mu n} + N L_{\mu n} &= -\frac{\eta}{h_\mu} \left(\mu \frac{\partial Q_n}{\partial \mu} + n Q_n \right) - \frac{1}{\beta} V_{\mu n}, \\ \frac{\partial g_{\eta n}}{\partial t} + G_{\eta n} + N L_{\eta n} &= -\frac{\mu}{h_\eta} \left(\eta \frac{\partial Q_n}{\partial \eta} + n Q_n \right) - \frac{1}{\beta} V_{\eta n}, \\ \frac{\partial g_{\theta n}}{\partial t} + G_{\theta n} + N L_{\theta n} &= -\frac{i n Q_n \mu \eta}{h_\theta} - \frac{1}{\beta} V_{\theta n}. \end{aligned} \right\} \tag{17}$$

The nonlinear $NL_{\mu n}$ term, coming from the contribution $\boldsymbol{\omega} \times \boldsymbol{v}|_{\mu n}$ in (5a), is

$$N L_{\mu n} = \frac{1}{\mu^2 \eta^2} \sum_{\substack{m,j \\ m+j=n}} (g_{\eta m} q_{\theta j} - q_{\theta m} g_{\eta j})(\mu \eta)^{|m+j|-(m+j)}, \tag{18}$$

and similarly for $NL_{\eta n}$ and $NL_{\theta n}$. The viscous term $V_{\mu n}$ is

$$V_{\mu n} = \frac{1}{h_\eta h_\theta} \left[\frac{1}{\mu} \frac{\partial}{\partial \eta} \left(\frac{h_\theta q_\theta}{\eta} \right) + (n-1) \frac{h_\theta q_\theta}{\mu \eta^2} - i n \frac{h_\eta q_\eta}{\mu \eta} \right]. \tag{19}$$

The G_{kn} linear terms due to the coordinate motion are easily derived from the original formulation. The boundary conditions at the wall and at the inlet plane (7) are rewritten in terms of the scaled variables.

The evolution equations (17) for the harmonics g_{kn}, with boundary conditions (12)–(14), correspond to the Navier–Stokes equation in terms of primitive variables incorporating all the regularity conditions (8) at the singular axis.

3. Numerical method

The mathematical problem described in §2 is solved numerically. In the meridian plane $\{\mu, \eta\}$, the flow equations are made discrete on a face-centred staggered grid with standard second-order finite differences. A fractional step method is used for the time advancement following Verzicco & Orlandi (1996), where the intermediate

non-soleinodal field is evaluated using the current irrotational contribution. The intermediate field $\hat{g}$ is obtained using a low-storage third-order Runge–Kutta explicit scheme. Once the intermediate non-soleinodal field $\hat{g}$ is known, the mass conservation law is enforced by solving Poisson-type equations for the corrections ΔQ_n of the pseudopotential harmonics Q_n. The procedure can be summarized as

$$\hat{g}_{kn} = g_{kn}(t) + \Delta g_{kn},$$
$$\mathscr{D}\hat{g}_n = \mathscr{D}\mathscr{G}(\Delta Q_n(t + \Delta t)),$$
$$g_{kn}(t + \Delta t) = \hat{g}_{kn} - \mathscr{G}_k(\Delta Q_n(t + \Delta t)),$$
$$Q_n(t + \mathrm{d}t) = Q_n(t) + \Delta Q_n(t + \Delta t) + O(\Delta t/\beta),$$

where Δg_{kn} indicates symbolically the time advancement of (17), $\mathscr{G}$ and $\mathscr{D}$ are the discrete versions of the formal gradient (16) and divergence operators, respectively, and the subscripts n and k have the same meaning as in equation (9). Attention has been paid that the discrete curl operator $\mathscr{C}$ (giving q_{kn} when applied to g_{kn}) is defined congruently to the discrete gradient operator $\mathscr{G}$ in order to satisfy the discrete differential identity $\mathscr{C}(\mathscr{G}f) = 0$, where f is an arbitrary scalar field. Note that, because of the grid motion, the operators, and therefore the coefficients of the linear system operator $\mathscr{D}\mathscr{G}$, must be updated at each time step. The presence of the irrotational (pressure) term in Δg_n, see equations (5a) and (17), allows the instantaneous boundary conditions to be imposed on the $\hat{g}$ field (Verzicco & Orlandi 1996). The Poisson-type equations are then solved by imposing instantaneous impenetrability at the boundaries, and the regularity conditions (13) at the axis.

At $t = 0$, the flow is assumed to start from rest; the initial value $\delta(0)$ is computed from $H(0)$ and $D(0)$, and then updated during computation.

The nonlinear term (18) is computed with a direct convolution in the Fourier space or, alternatively, in the physical domain using a zero-padding technique (Canuto *et al.* 1988), giving indistinguishable results; the method is selected to optimize the speed depending on the number of harmonics effectively solved (see Domenichini & Baccani 2004 for estimates in an analogous method in cylindrical coordinates).

In the meridian plane, the resolution employed is $[N_\mu \times N_\eta] = [96 \times 128]$, N_μ and N_η being the number of computational cells in the μ- and η-directions, respectively. Stretched grids are used to improve resolution near the walls and the mitral plane; details can be found in Baccani *et al.* (2002a). Grid refinement studies have been performed by varying numerical parameters and resolution up to $[128 \times 160]$ to verify that the results are not influenced by the numerics. In the azimuthal direction, the number N_θ of the effectively solved harmonics has been varied; the results reported in what follows are obtained with $N_\theta = 12$ (corresponding to 16 harmonics when the zero-padding technique is used); depending on the value of the eccentricity ε, a smaller number of harmonics proved to be sufficient in these ranges of physical parameters. The time step Δt is selected to satisfy the convective and diffusive stability criteria, the latter being the more restrictive (especially close to the focus of the coordinate system); the results have been obtained with Δt values from 2^{-12} up to 2^{-15} in the most viscous (low-β) cases.

4. Results

The system has been analysed by varying the eccentricity ε of the inlet profile (7) in the range from 0.02 to 0.125. The Stokes number β was considered in the interval between 64 and 144, the Strouhal number was first set at $St = 0.072$ and then reduced
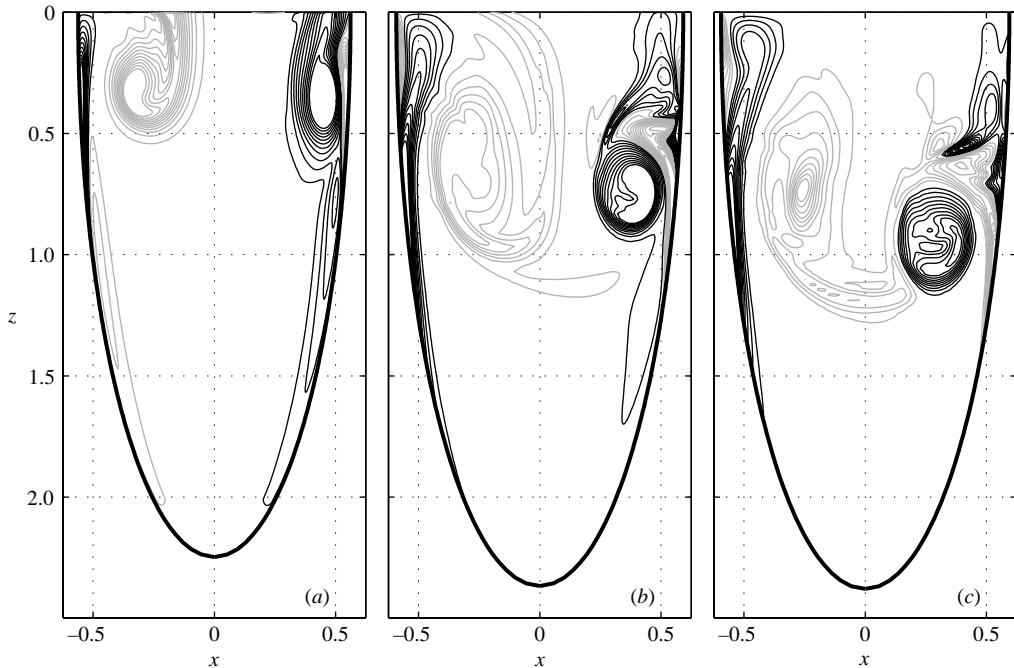
FIGURE 2. Distribution of ω_y on the symmetry plane, $St = 0.072$, $\beta = 144$, $\varepsilon = 0.125$; (*a*) $t = 20/128$, (*b*) $t = 40/128$, (*c*) $t = 50/128$. Levels from -262.5 to 262.5, step 25; positive values black, negative values grey.

to 0.05. The case $\beta = 144$, $St = 0.072$, $\varepsilon = 0.125$ is discussed as a reference one; the results are then compared to those obtained with different values of the parameters.

The axisymmetric geometry and the inlet velocity profile (7) result in the presence of a symmetry plane, the plane $\sin \theta = 0$. The presence of a symmetry plane is a useful feature for the analysis of the results (Bolzon *et al.* 2002), because the velocity has no component normal to it and the only non-zero vorticity is ω_θ. In order to facilitate readability, when the flow evolution on the symmetry plane is described, the Cartesian component ω_y is plotted in place of ω_θ.

4.1. *Flow evolution for $\beta = 144$, $St = 0.072$, $\varepsilon = 0.125$*

In figure 2, the evolution of ω_y on the symmetry plane is reported. During the initial stage of the motion, most of the flow is irrotational, with the exception of the viscous boundary layer at the cavity wall and of a well-defined vortex structure close to the entrance. This structure is a ring-shaped vortex, whose geometry is strictly related to the eccentricity of the entering velocity profile, as will be shown in §4.2. A picture of this initial period is shown in figure 2(*a*), $t = 20/128$, where the right (counterclockwise, black in the figure) portion of the vortex extends along the ventricle wall, while the left portion develops a roll-up in the central part of the cavity. An opposite-sign vortex-induced boundary layer at the wall is found on both sides and the vorticity distribution is very similar to what would be expected in a two-dimensional problem. During the following evolution, when the entry flow decelerates, the right compact part of the vortex structure strongly interacts with the vortex-induced boundary layer that separates with the appearance of a third vorticity layer, figure 2(*b*), $t = 40/128$. On the opposite side, the main compact structure grows in size, and interacts more
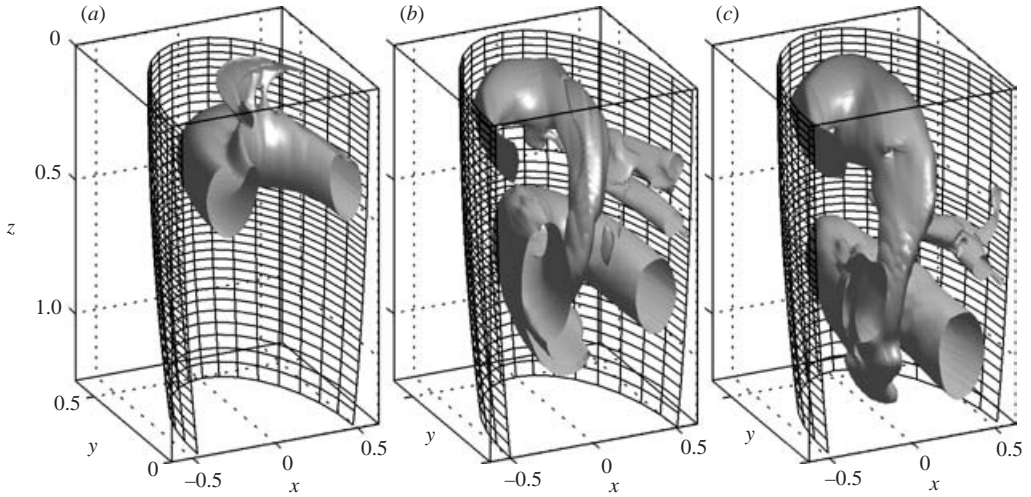
FIGURE 3. Isosurface of λ_2, $St = 0.072$, $\beta = 144$, $\varepsilon = 0.125$; (a) $t = 20/128$, (b) $t = 40/128$, (c) $t = 50/128$. Value: -1000.

weakly with the boundary layer moving toward the centre of the cavity. Here we start to see evidence of an evolution that is driven by out-of-plane phenomena. The shear layer that connects the inlet to the leading vortex (left side of the figure) rapidly extends in the rightward direction instead of rolling-up around the vortex itself, as would be expected in a two-dimensional flow, and eventually stretches around the compact right-side vorticity, figure 2(c), $t = 50/128$. During the final period, the picture does not differ significantly from that in figure 2(c); the very low values of the forcing discharge do not induce further appreciable growth of the ventricle size, and the vortex wake remains almost in the same position. Such a final evolution has little practical relevance, because at this stage of the deceleration the pulse is replaced by the following physiological phase (atrial or ventricular contraction).

An understanding of the three-dimensional dynamics can be obtained from figure 3, where isosurfaces of λ_2 are reported. Following Jeong & Hussain (1995), the scalar function λ_2 is the intermediate eigenvalue of the symmetric tensor $\mathbf{S}^2 + \mathbf{\Omega}^2 = S_{ik}S_{kj} + \Omega_{ik}\Omega_{kj}$, where $\mathbf{S}$ and $\mathbf{\Omega}$ are the symmetric and antisymmetric part of the velocity gradient, respectively. A vortex structures is commonly identified by extreme negative values of λ_2 (roughly corresponding to local pressure minima due to vortical motion). The structure close to the inlet section initially appears as a well-defined ring-shaped vortex, figure 3(a). At this stage, the vorticity field is still dominated by its θ-component and we can expect that positive and negative spots of ω_y on the symmetry plane, figure 2, roughly connect with each other with nearly circular vortex lines. The vortex-induced boundary layer at the wall is a shear layer still not organized in a compact structure. Nevertheless, some vorticity reconnection between the ring-like vortex and the opposite-sign boundary layer vorticity at the nearest wall (on the right, either in figure 2a or 3a) is taking place (Kida & Takaoka 1994; Bolzon *et al.* 2003). Afterwards, as shown in figure 3(b) (see also figure 2b), the boundary layer structure develops into an incomplete ring near the wall: vortex lines coming from the left-side wall ($\theta \simeq \pi$) do not close on the boundary layer vorticity, that ($\theta \simeq 0$ and $z \simeq 0.5$) has paired with nearby wake vorticity, and must connect with the main vortex structure, deviating towards the centre of the cavity and downstream. This process produces
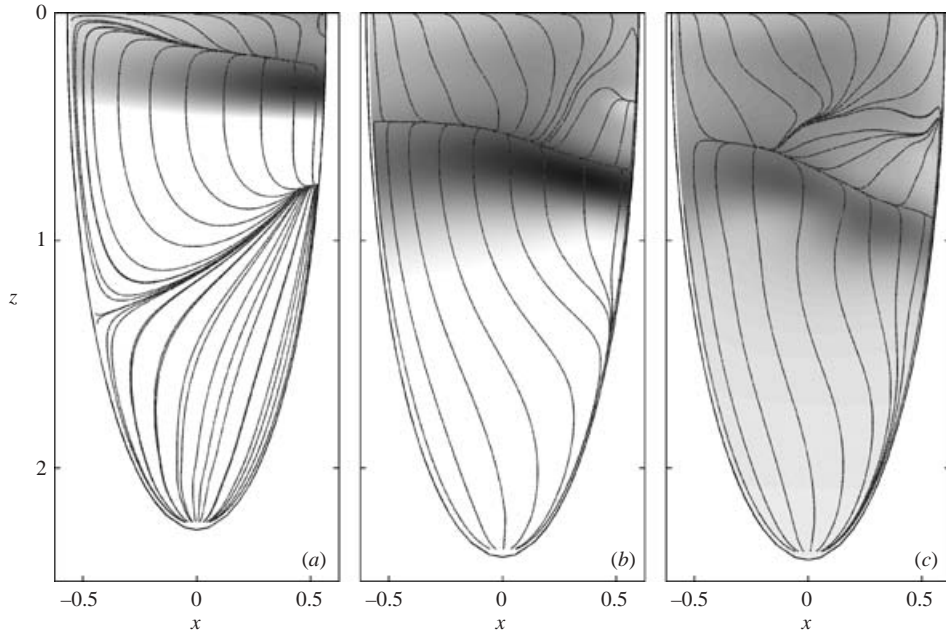
FIGURE 4. Pressure distribution at the wall and limiting streamlines pattern, $St = 0.072$, $\beta = 144$, $\varepsilon = 0.125$; (a) $t = 20/128$, (b) $t = 40/128$, (c) $t = 50/128$. Pressure values from -10 (white) to 30 (dark grey).

a significant z-component of the vorticity field in the central region of the ventricle. The three-dimensional organization of the vorticity field shows some persistence, and does not change its shape qualitatively during the following evolution until the end of computations, figure 3(c).

The signature of this flow evolution on the wall is shown in figure 4: the relative pressure distribution at the wall is reported in grey scale together with the limiting streamlines pattern (this is the front view of the actual three-dimensional pattern computed on the cavity wall). The flow at the wall, figure 4(a), is initially divided into three distinct zones: in the lowest part, close to the apex, the bulk irrotational flow is driven by the wall motion, the pressure is almost constant and the limiting streamlines are the trace of the forming boundary layer. The middle region corresponds to the vortex-induced boundary layer where the wall stress is adverse to the entering flow. The lower dividing line (approximately from $z \simeq 0.8$ at $\theta = 0$ to $z \simeq 1.3$ at $\theta = \pi$) is a reattachment line while the upper dividing line is a separation one (approximately from $z \simeq 0.25$ at $\theta = 0$ to $z \simeq 0$ at $\theta = \pi$: here the azimuthal component of the wall stress is negative, that is the limiting streamlines travel from $\theta = \pi$ to $\theta = 0$). The pressure distribution presents a band of local maxima downstream of the separation line ($z \simeq 0.2$), which divides the inlet zone, with adverse pressure gradient, from the favourable pressure gradient downstream. At $t = 40/128$, the reattachment line has disappeared, depending on the inversion of the wall vorticity due to the flow deceleration. At this stage and afterwards, the boundary layer separation loses its quasi-two-dimensional appearance (separation–attachment): a local wall structure develops from $\theta = 0$ and $z \simeq 0.4$ in correspondence with the vorticity reconnection; it gives a relative minimum of pressure while the maxima are still downstream of the separation line. During the following evolution, the separation line slightly deforms in
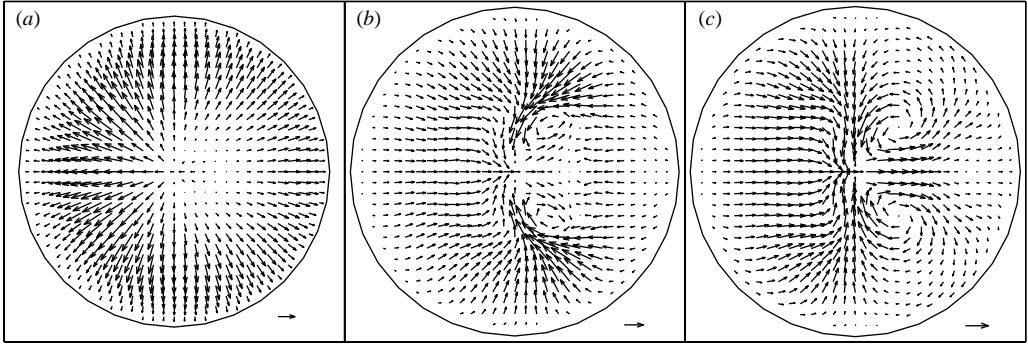
FIGURE 5. Velocity field, x, y-projection; $St = 0.072$, $\beta = 144$, $\varepsilon = 0.125$ at $z = 0.5$; (a) $t = 20/128$, (b) $t = 40/128$, (c) $t = 50/128$. The external arrows indicate the length of 5 velocity units.

accordance with the main structure dynamics while the lines starting from the focus at $\theta = 0$, $z \simeq 0.5$, extend along the azimuthal direction up to about half the cavity, figure 4(c), being related to the growth of the ω_z component of the main vortex.

The development of the vertical vorticity component gives rise to secondary flows. In figure 5 we report the x, y-projection of the velocity field on the cross-section at $z \simeq 0.5$. At $t = 20/128$, the jet head has not yet reached the plane $z \simeq 0.5$ where the secondary flow is divergent due to the enlargement of the available area, figure 5(a), and the flow pattern is directly connected to the eccentricity of the entering jet. At $t = 40/128$, a similar pattern would be found in correspondence with the head of the leading vortex structure, say $z \gtrsim 1$, while upstream of the vortex head, figure 5(b), the flow is dominated by the two legs of the vortex structure (compare with figure 3b), whose z-component gives rise to two localized circulating cells, at $r \simeq 0.25$ and $\theta \simeq \pm \pi/4$ (Bolzon *et al.* 2003). A similar pattern can be observed at $t = 50/128$, figure 5(c); the legs of the vortex structure elongate following the motion of the head, see figure 3(c), and approach each other moving towards the symmetry plane.

The overall structure is that of a ring-shaped vortex, that is wider on the side next to the closed part of the entrance (after the longer leaflet) and more compact but still intense on the opposite side where its core is closer to the apex, and two vertical legs connect it to an incomplete ring wall structure behind the longer leaflet.

4.2. *Influence of parameters β and ε*

In figure 6, the ω_y distributions on the symmetry plane at $t = 50/128$ are reported for four different cases, where in each picture only one parameter is changed from what is shown in figure 2(c). In the analysed range, the flow evolution is not significantly affected by the Stokes parameter: the same vorticity structure detected in the case $\beta = 144$ is recognizable in figures 6(a) and 6(b) corresponding to $\beta = 64$ and $\beta = 81$, respectively. Lower values of the Stokes number give smoother flow fields without affecting the vorticity structure qualitatively. The variation of the eccentricity directly corresponds to a variation of the flow geometry starting from the case $\varepsilon = 0.02$, figure 6(c), that does not differ significantly from the axisymmetric solution (Baccani *et al.* 2002a). A progressive growth of the three-dimensionality can be observed through the case $\varepsilon = 0.05$, figure 6(d), to the flow found for $\varepsilon = 0.125$. The transition is continuous and does not show any appearance of instabilities.

The same conclusions can be drawn from figure 7, where the distributions of λ_2 are reported for the same fields shown in figure 6. The weak dependence of the solution on the Stokes number is confirmed by the vortex structures in figures 7(a) and 7(b). The
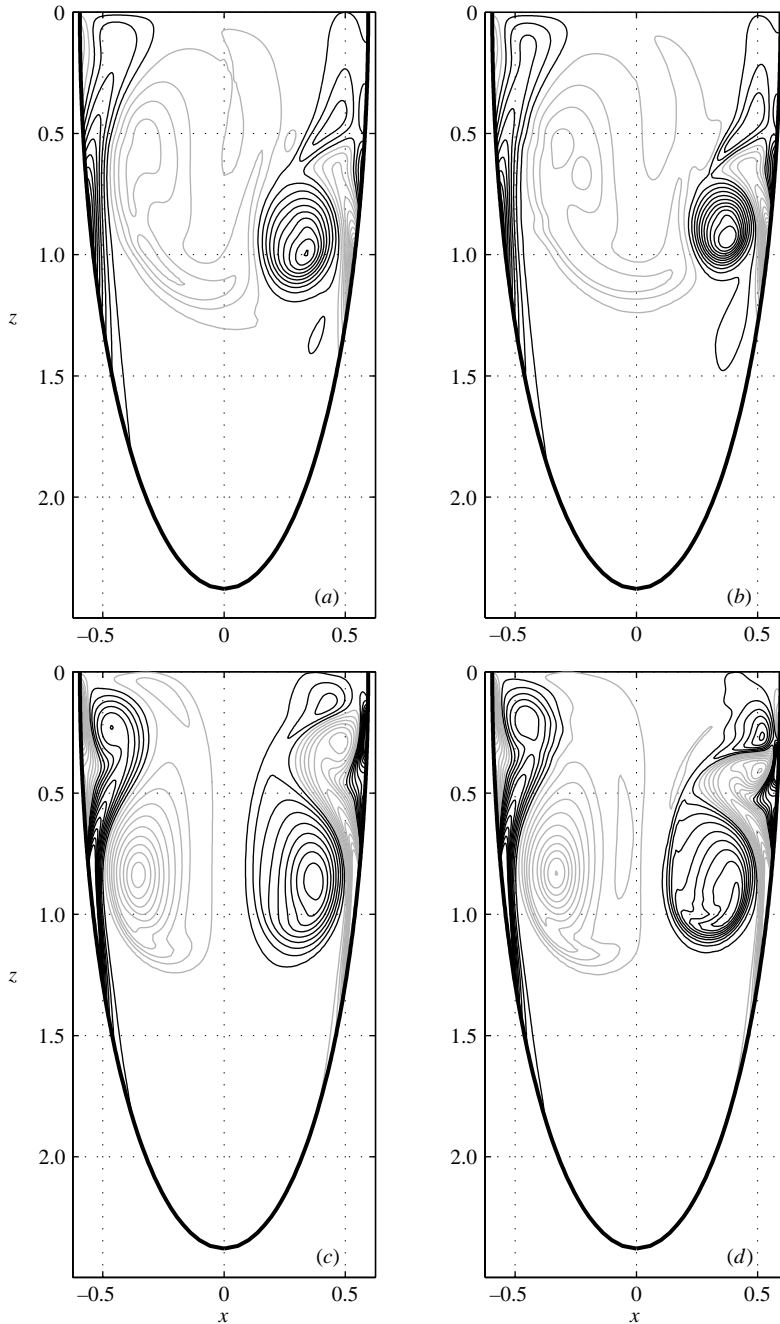
FIGURE 6. Distribution of ω_y on the symmetry plane, $St = 0.072$, $t = 50/128$; (a) $\beta = 64$, $\varepsilon = 0.125$, (b) $\beta = 81$, $\varepsilon = 0.125$, (c) $\beta = 144$, $\varepsilon = 0.02$, (d) $\beta = 144$, $\varepsilon = 0.05$. Levels from -262.5 to 262.5, step 25; positive values black, negative values grey.

case $\varepsilon = 0.02$ shows a weakly asymmetric vorticity field, where the main vortex ring structure and the opposite-sign boundary layer one are still quite distinct, figure 7(c); the loss of coherence of the boundary layer vortex ring, which tends to connect to the leading vortex structure, becomes more evident in figure 7(d), $\varepsilon = 0.05$.
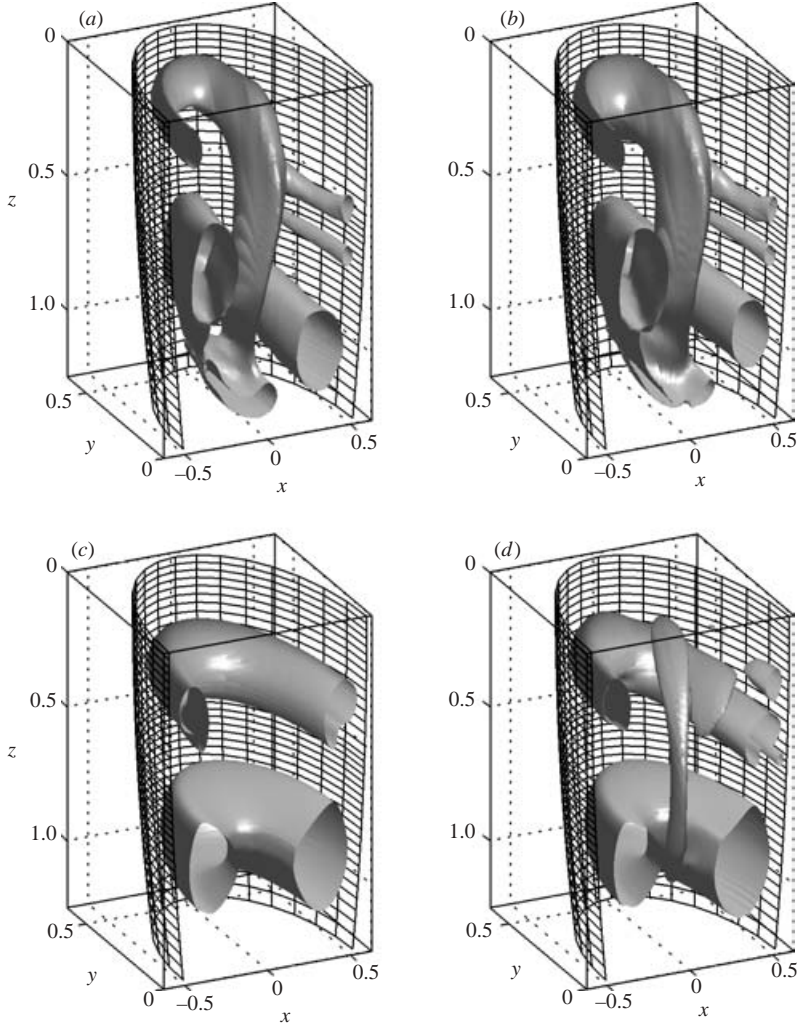
FIGURE 7. Isosurface of λ_2, $St = 0.072$, $t = 50/128$; (a) $\beta = 64$, $\varepsilon = 0.125$, (b) $\beta = 81$, $\varepsilon = 0.125$, (c) $\beta = 144$, $\varepsilon = 0.02$, (d) $\beta = 144$, $\varepsilon = 0.05$. Value: (a) and (b) -300, (c) and (d) -1000.

4.3. *Influence of the Strouhal number*

From the results reported so far, the flow evolution is directly related to the eccentricity of the entering jet, while the Stokes number does not play a primary role. The influence of the other flow parameter, i.e. the Strouhal number, has been analysed by fixing $\beta = 81$, $\varepsilon = 0.125$, and reducing the Strouhal number to $St = 0.05$. The results are reported in figure 8 in terms of the vorticity evolution on the symmetry plane. The comparison with the similar fields in figure 2 immediately shows the increased relevance of the convective phenomena: the entering jet penetrates the cavity further downstream affecting the initial evolution in a quantitative manner, figure 8(a); nevertheless from a qualitative point of view the initial picture is not significantly different from that of figure 2(a). More relevant differences are detected afterwards. The leading vortex structure rapidly reaches the narrower region of the cavity, becoming therefore more constrained by the presence of the wall. The vortex sheet connecting the left-side vortex to the entrance elongates to the right
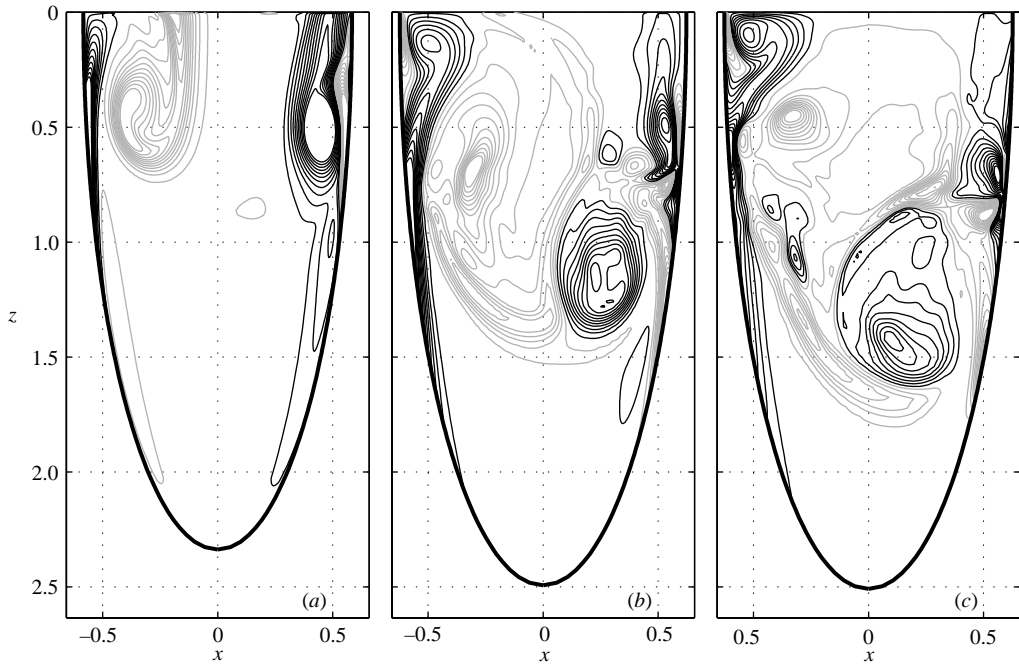
FIGURE 8. Distribution of ω_y on the symmetry plane, $St = 0.05$, $\beta = 81$, $\varepsilon = 0.125$; (a) $t = 20/128$, (b) $t = 40/128$, (c) $t = 50/128$. Levels from -262.5 to 262.5, step 25; positive values black, negative values grey.
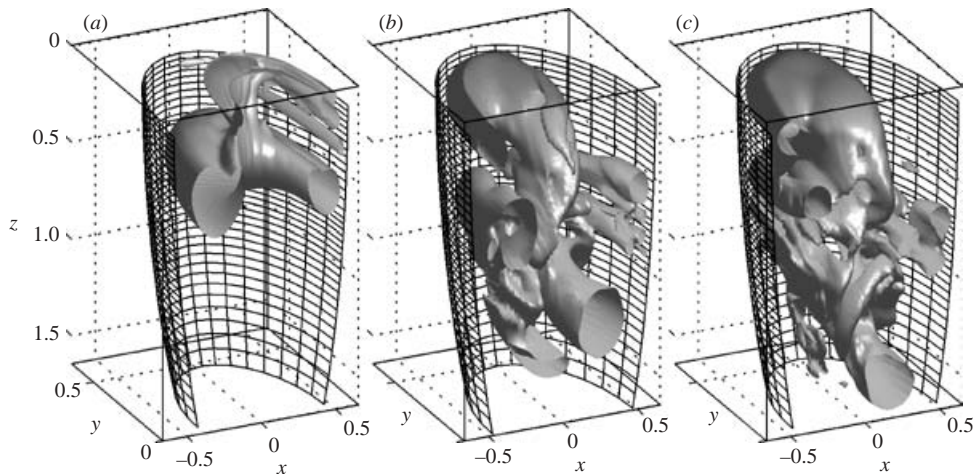

FIGURE 9. Isosurface of λ_2, $St = 0.05$, $\beta = 81$, $\varepsilon = 0.125$; (a) $t = 20/128$, (b) $t = 40/128$, (c) $t = 50/128$. Value: -1000.

and is stretched further downstream by the opposite-side vorticity, see figure 8(b) at $t = 40/128$, therefore anticipating and increasing the intensity of the phenomena observed in the case $St = 0.072$. This dynamics continues when the two opposite sides move almost transversally to the cavity axis, figure 8(c) at $t = 50/128$.

The distributions of λ_2 in figure 9 show the evolution of the vorticity field from the initial ring-like shape to the final complex three-dimensional one, when the cavity is
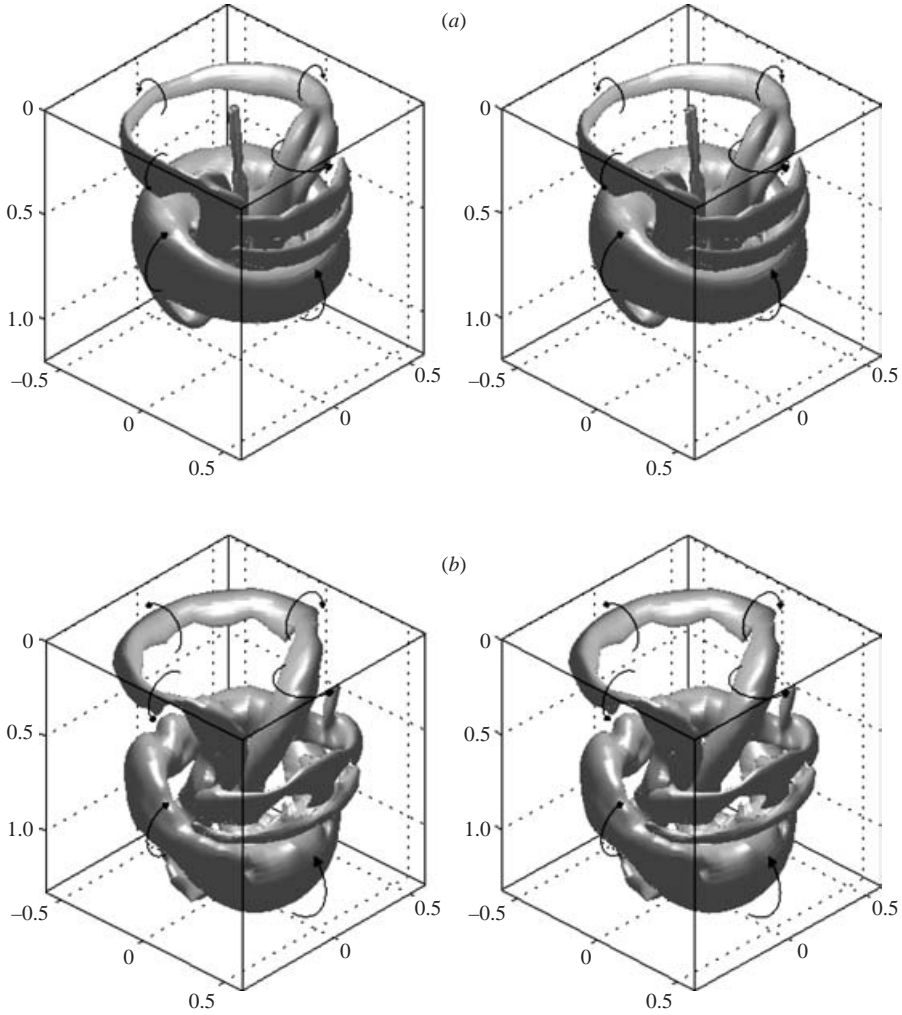
FIGURE 10. Stereoscopic view of the isosurface of λ_2, $t = 38/128$, $\varepsilon = 0.125$. $\beta = 81$.
(*a*) $St = 0.072$, value: -500; (*b*) $St = 0.05$, value: -5000.

almost completely filled by knotted vortex structures. The progressive loss of regularity
is accompanied by the transition to a weakly turbulent field in the central region of
the ventricle. The loss of coherence is not accompanied or preceded by the growth of
different structures. The unique coherent structure is the same as found in the previous
cases, and afterward the flow undergoes a transition to a weak turbulent regime whose
development prevents the computation being extended being extended to lower values
of the Strouhal number within our present DNS resolution capabilities.

Stereoscopic views of the complete λ_2 fields at $t = 38/128$ are reported in figure 10,
for $\varepsilon = 0.125$ and $\beta = 81$, at $St = 0.072$ (*a*) and $St = 0.05$ (*b*). As previously discussed,
at lower St the convective phenomena are more relevant, elongating the entering jet
inside of the cavity and enhancing the interaction between the main vortex structure
and the wall, but, notwithstanding the differences between the fields in figure 10, a
common evolution has been observed. During the accelerating phase, a single vortex
structure develops at the inlet. Such a unique structure interacts with the boundary
layer, inducing a wall vortex ring. The vorticity reconnection progressively disrupts

the wall vortex on one side while the opposite side reconnects to the leading vortex with the development of two legs of vertical vorticity. The birth of a significant ω_z component gives rise to secondary flows, which detach the boundary layer structure from the wall and drive it towards the centre of the cavity, until the final stage of the evolution with the persistent knotted structures in figure 10.

The formation of a single ring-shaped vortex structure at the inlet section can be investigated in terms of the formation number $F(t) = L(t)/d(t)$, where $d(t) = \sigma D(t)$ is the time-varying diameter of the entering jet, and

$$L(t) = \int_0^t \frac{4\mathscr{Q}(t)}{\pi D(t)^2 \sigma^2} \, \mathrm{d}t$$

in the present context plays the role of the piston stroke (Gharib, Rambod & Shariff 1998). It has been proven that in the case of an impulsively started jet generated by a piston in a water tank, $F \simeq 4$ is the limiting value that divides the generation of a single vortex from that of a leading ring followed by a trailing jet. In the present problem and for the studied cases, F is always smaller than 4, a value that can be reached corresponding to the lowest physiological Strouhal numbers. For example, at $St \simeq 0.047$ the value $F = 4$ is reached at the end of the computation, $t = 0.5$, while for $St = 0.035$ F becomes larger than 4 at $t \simeq 0.2$, but its maximum at $t = 0.5$ is approximately 4.7. Furthermore the limiting value is expected to increase when the inflow is smoother than that of a piston stroke in rigid walls.

There are several differences between the present problem and that of a piston-driven jet; however these results and clinical data from healthy subjects (Garcia *et al.* 1998) would suggest that the actual left ventricle filling flow does not differ significantly from that described here. Possibly, the single vortex structure corresponds to a physiological optimization, like for example a minimal muscular strength in the following ejection, as argued by Gharib *et al.* (1998). In any case, this flow regime is found to be at the edge of the development of weak turbulence and a further reduction of the Strouhal number, especially if β is increased, can qualitatively modify the dynamics and its influence on the tissue.

5. Conclusions

A numerical analysis of the three-dimensional flow inside an expanding cavity modelling the diastolic filling of the left ventricle has been presented. An original mathematical method to deal with the Fourier representation of the flow equations in axisymmetric systems of coordinates has been introduced, and implemented in the numerical framework. The simple geometry of the model allows an accurate numerical solution, based on a mixed spectral–finite differences method. Alternatively, a spectral approach could be used in the meridian plane too, by expansion in terms of Chebyshev and Legendre polynomial or prolate spheroidal wavefunctions, that automatically satisfy the regularity conditions at the axis. These techniques are in principle very accurate although not commonly straightforward. On another side they cannot be easily generalized to other than the basic domains and boundary conditions.

The problem has been analysed for values of the geometrical and flow parameters corresponding to those of a left ventricle in healthy young adults. The entering flow organizes into a single eccentric ring-shaped vortex structure corresponding to the head of the mitral jet. The vortex-induced boundary layer develops into an incomplete ring structure that connects with the main vortex through two legs of almost vertical vorticity.

The solution is directly dependent on the properties of the entering jet. At growing values of the eccentricity the flow field changes smoothly from almost axisymmetric to the three-dimensional structures when values are comparable with the physiological ones. The solution has shown a weak dependence on the Stokes number whose influence is limited to the smoothness of the flow field.

The Strouhal number has an important influence on the solution. For decreasing values, the relative contribution of convection increases, and the entry jet extends more deeply into the ventricle and eventually may become unstable, developing weak turbulence. The vortex structure of a single ring connected to the incomplete wake-induced ring in the boundary layer seems to be persistent. This can be justified by the value of the formation number (Gharib *et al.* 1998), which does not exceed the critical value for the formation of a multiple vortex wake. This type of coherent vortex structure remains the dominant flow feature before the development of weak turbulence.

The pattern found is in qualitative agreement with that observed *in vivo* and in experimental studies (Bellhouse 1972; Reul *et al.* 1981; Kim *et al.* 1995; Kilner *et al.* 2000; Vlachos *et al.* 2001), notwithstanding the differences between the present model and an actual ventricle. The main circulating region commonly found – in planar visualizations – behind the longer valvular side represents one part of the vortex ring structure. The other part, which is smaller and closer to the wall near the apex, is often not immediately visible although it is always present.

The results indicate that healthy ventricular flow is at the edge of developing weak turbulence. This could correspond to the complex pattern in colour Doppler imaging often recorded in echographic measurements. We can expect that some turbulence will develop in the presence of pathologies that decrease the Strouhal number, especially when β is large.

This analysis has been performed with simplified although fairly realistic model and parameters. Notwithstanding the accuracy and the overall agreements, the present work represents a basic and preliminary study in the understanding of the main fluid dynamics involved in the left ventricular flow.

A limitation of this study is the assumption of a quiescent flow as initial condition. A real cardiac cycle is made up of a first pulse (the early filling), the one here considered, a second filling pulse (the atrial contraction), which is weaker in healthy conditions, followed by the ejection of flow during the systolic contraction. Indeed, the flow is not completely vorticity-free before filling starts and the assumption adopted, which represents an approximation, is taken for the sake of understanding the basic diastolic structure. However, Nakamura *et al.* (2004) have shown that the vortex structure is only weakly affected by flow disturbances remaining at the onset of diastole, and such an influence is also limited to the first, accelerating, phase. That work and our preliminary studies of the entire cardiac cycle show that the diastolic vortex structure is highly stretched during systole and it is ejected or dissipated almost completely before the diastole begins. The vorticity remaining from the previous cycle is, commonly, extremely weak although its distribution depends on the type of outflow and systolic arrangement. Further steps are necessary to analyse sequences of complete heart beat periods in specific conditions, and to include the influence of the actual moving-leaflet valvular dynamics.

REFERENCES

BACCANI, B., DOMENICHINI, F. & PEDRIZZETTI, G. 2002*a* Vortex dynamics in a model left ventricle during filling. *Eur. J. Mech.* B/*Fluids* **21**, 527–543.

BACCANI, B., DOMENICHINI, F. & PEDRIZZETTI, G. 2003 Model and influence of mitral valve opening during the left ventricular filling. *J. Biomech.* **36**, 355–361.

BACCANI, B., DOMENICHINI, F., PEDRIZZETTI, G. & TONTI, G. 2002*b* Fluid dynamics of the left ventricular filling in dilated cardiomyopathy. *J. Biomech.* **35**, 665–671.

BATCHELOR, G. K. 1967 *An Introduction to Fluid Dynamics.* Cambridge University Press.

BELLHOUSE, B. J. 1972 Fluid mechanics of a model mitral valve and left ventricle. *Cardiovas. Res.* **6**, 199–210.

BOLZON, G., PEDRIZZETTI, G., GRIGIONI, M., ZOVATTO, L., DANIELE, C. & D'AVENIO, G. 2002 Flow on the symmetry plane of a total cavo-pulmonary connection. *J. Biomech.* **35**, 595–608.

BOLZON, G., ZOVATTO, L. & PEDRIZZETTI, G. 2003 Birth of three-dimensionality in a pulsed jet through a circular orifice. *J. Fluid Mech.* **493**, 209–218.

CANUTO, C., HUSSAINI, M. Y., QUARTERONI, A. & ZANG, T. 1988 *Spectral Methods in Fluid Dynamics.* Springer.

CONSTANTINESCU, G. S. & LELE, S. K. 2002 A highly accurate technique for the treatment of flow equations at the polar axis in cylindrical coordinates using series expansions. *J. Comput. Phys.* **183**, 165–186.

DOMENICHINI, F. & BACCANI, B. 2004 A formulation of Navier-Stokes problem in cylindrical coordinates applied to the 3D entry jet in a duct. *J. Comput. Phys.* **200**, 177–191.

GARCIA, M. J., THOMAS, J. D. & KLEIN, A. L. 1998 New Doppler echocardiographic applications for the study of diastolic function. *J. Am. Coll. Cardiol.* **32**, 865–875.

GHARIB, M., RAMBOD, E. & SHARIFF, K. 1998 A universal time scale for vortex ring formation. *J. Fluid Mech.* **360**, 121–140.

JEONG, J. & HUSSAIN, F. 1995 On the identification of a vortex. *J. Fluid Mech.* **285**, 69–94.

KIDA, S. & TAKAOKA, M. 1994 Vortex reconnection. *Annu. Rev. Fluid Mech.* **26**, 169–177.

KILNER, P. J., YANG, G. Z., WILKES, A. J., MOHIADDIN, R. H., FIRMIN, D. N. & YACOUB, M. H. 2000 Asymmetric redirection of flow through the heart. *Nature* **404**, 759–761.

KIM, W. Y., WALKER, P. G., PEDERSON, E. M., POULSEN, J. K., OYRE, S., HOULIND, K. & YOGANATHAN, A. P. 1995 Left ventricular blood flow patterns in normal subjects: a quantitative analysis by three-dimensional magnetic resonance velocity mapping. *J. Am. Coll. Cardiol.* **26**, 224–238.

LEMMON, J. D. & YOGANATHAN, A. P. 2000 Three-dimensional computational model of left heart diastolic function with fluid-structure interaction. *J. Biomech. Engng* **122**, 109–117.

LEWIS, H. R. & BELLAN, P. M. 1990 Physical constraints on the coefficients of Fourier expansions in cylindrical coordinates. *J. Math. Phys.* **31**, 2592–2596.

LOPEZ, J. M., MARQUES, F. & SHEN, J. 2002 An efficient spectral-projection method for the Navier-Stokes equations in cylindrical geometries. *J. Comput. Phys.* **176**, 384–401.

MANDINOV, L., EBERLI, F. R., SEILER, C. & HESS, O. M. 2000 Review: Diastolic heart failure. *Cardiovas. Res.* **45**, 813–825.

MCQUEEN, D. M. & PESKIN, C. S. 2000 A three-dimensional computer model of the human heart for studying cardiac fluid dynamics. *Computer Graphics* **34**, 56–60.

MORSE, P. M. & FESHBACH, H. 1953 *Methods of Theoretical Physics.* McGraw-Hill.

NAKAMURA, M., WADA, S., MIKAMI, T., KITABATAKE, A. & KARINO, T. 2003 Computational study on the evolution of an intraventricular vortical flow during early diastole for the interpretation of color M-mode Doppler echocardiograms. *Biomech. Model. Mechanobiol.* **2**, 59–72.

NAKAMURA, M., WADA, S., MIKAMI, T., KITABATAKE, A., KARINO, T. & YAMAGUCHI, T. 2004 Effect of flow disturbances remaining at the beginning of diastole on intraventricular diastolic flow and colour M-mode Doppler echocardiograms. *Med. Biol. Engng Comput.* **42**, 509–515.

PESKIN, C. S. & MCQUENN, D. M. 1989*a* A three-dimensional computational method for blood flow in the heart: I Immersed elastic fibers in an incompressible fluid. *J. Comput. Phys.* **81**, 372–405.

Peskin, C. S. & McQuenn, D. M. 1989*b* A three-dimensional computational method for blood flow in the heart: II Contractile fibers. *J. Comput. Phys.* **82**, 289–298.

Reul, H., Talukder, N. & Muller, W. 1981 Fluid mechanics of the natural mitral valve. *J. Biomech.* **14**, 361–372.

Saber, N. R., Gosman, A. D., Wood, N. B., Kilner, P. J., Charrier, C. L. & Firmin, D. N. 2001 Computational flow modeling of the left ventricle based on in vivo MRI data: initial experience. *Ann. Biomed. Engng* **29**, 275–283.

Steen, T. & Steen, S. 1994 Filling of a model left ventricle studied by colour M mode Doppler. *Cardiovas. Res.* **28**, 1821–1827.

Stevens, C., Remme, E., LeGrice, I. & Hunter, P. 2003 Ventricular mechanics in diastole:material parameter sensitivity. *J. Biomech.* **36**, 737–748.

Taylor, T. W. & Yamaguchi, T. 1995 Realistic three-dimensional left ventricular ejection determined from computational fluid dynamics. *Med. Engng Phys.* **17**, 602–608.

Vasan, R. S. & Levy, D. 2000 Defining diastolic heart failure. *Circulation* **101**, 2118–2121.

Verzicco, R. & Orlandi, P. 1996 A finite-difference scheme for three-dimensional incompressible flows in cylindrical coordinates. *J. Comput. Phys.* **123**, 402–414.

Vierendeels, J. A., Dick, E. & Verdonck, P. R. 2002 Hydrodynamics of color M-mode Doppler flow wave propagation velocity V(p): A computer study. *J. Am. Soc. Echocardiogr.* **15**, 219–224.

Vierendeels, J. A., Riemslagh, K., Dick, E. & Verdonck, P. R. 2000 Computer simulation of intraventricular flow and pressure during diastole. *J. Biomech. Engng* **122**, 667–674.

Vlachos, P. P., Pierrakkos, O., Phillips, A. & Telionis, D. P. 2001 Vorticity and turbulence characteristics inside a transparent flexible left ventricle. BED-Vol. 50, pp. 493–494. ASME.

Wieting, D. W. & Stripling, T. E. 1984 Dynamics and fluid dynamics of the mitral valve. In *Recent Progress in Mitral Valve Disease* (ed. C. Duran, W. W. Angell, A. D. Johnson & J. H. Oury), pp. 13–46. Butterworths.